



## RESEARCH LETTER

10.1029/2019GL085056

## Key Points:

- We quantify the sensitivity of the deep ocean circulation to radiation and mixing efficiencies of internal tide-induced turbulent mixing
- The spatial patterns of deep diapycnal upwelling and downwelling are highly sensitive to the two efficiencies and their covariation
- The two efficiencies have to be changed in tandem to avoid significant inaccuracy in the quantification of deep branch of ocean circulation

## Supporting Information:

- Supporting Information S1

## Correspondence to:

L. Cimoli,  
laura.cimoli@physics.ox.ac.uk

## Citation:

Cimoli, L., Caulfield, C. P., Johnson, H. L., et al., & Vic, C. (2019). Sensitivity of deep ocean mixing to local internal tide breaking and mixing efficiency. *Geophysical Research Letters*, 43, 14,622–14,633. <https://doi.org/10.1029/2019GL085056>

Received 26 AUG 2019

Accepted 3 DEC 2019

Accepted article online 4 DEC 2019

Published online 30 DEC 2019

©2019. The Authors.

This is an open access article under the terms of the Creative Commons Attribution License, which permits use, distribution and reproduction in any medium, provided the original work is properly cited.

## Sensitivity of Deep Ocean Mixing to Local Internal Tide Breaking and Mixing Efficiency

Laura Cimoli<sup>1</sup>, Colm-cille P. Caulfield<sup>2</sup>, Helen L. Johnson<sup>3</sup>, David P. Marshall<sup>1</sup>, Ali Mashayek<sup>4</sup>, Alberto C. Naveira Garabato<sup>5</sup>, and Clément Vic<sup>6</sup>

<sup>1</sup>Department of Physics, University of Oxford, Oxford, UK, <sup>2</sup>BP Institute and Department of Applied Mathematics and Theoretical Physics, University of Cambridge, Cambridge, UK, <sup>3</sup>Department of Earth Sciences, University of Oxford, Oxford, UK, <sup>4</sup>Imperial College, London, UK, <sup>5</sup>National Oceanographic Centre, University of Southampton, Southampton, UK, <sup>6</sup>Université de Bretagne Occidentale, CNRS, IRD, Ifremer, Laboratoire d'Océanographie Physique et Spatiale (LOPS), IUEM, Plouzané, France

**Abstract** There have been recent advancements in the quantification of parameters describing the proportion of internal tide energy being dissipated locally and the “efficiency” of diapycnal mixing, that is, the ratio of the diapycnal mixing rate to the kinetic energy dissipation rate. We show that oceanic tidal mixing is nontrivially sensitive to the covariation of these parameters. Varying these parameters one at a time can lead to significant errors in the patterns of diapycnal mixing-driven upwelling and downwelling and to the over and under estimation of mixing in such a way that the net rate of globally integrated deep circulation appears reasonable. However, the local rates of upwelling and downwelling in the deep ocean are significantly different when both parameters are allowed to covary and be spatially variable. These findings have important implications for the representation of oceanic heat, carbon, nutrients, and other tracer budgets in general circulation models.

**Plain Language Summary** Deep ocean basins are filled with dense waters that form at high latitudes and sink to the abyss. The overturning circulation of the ocean, a key regulator of the climate system, is only feasible if such dense waters can resurface. The breaking of internal waves makes such resurfacing possible. In the deep ocean, internal waves are largely generated by the flow of tides over topography. Their breaking mixes dense deep waters with lighter waters above them, bringing them upward. Two key parameters in climate models for modeling such mixing are (I) the ratio of energy in the wave field that is spent near rough topography due to breaking as opposed to what is radiated away and (II) the amount of energy from wave breaking that goes to mixing versus what is wasted through dissipation by viscosity of seawater. Both parameters are considered constant in climate models. In this work, we quantify the roles of variations in each of these two parameters in setting the patterns of deep ocean upwelling of dense waters and argue that the two parameters need to be changed realistically and interdependently to avoid significant inaccuracies in the quantification of the mixing-induced deep branch of ocean circulation.

### 1. Introduction

The deep ocean circulation is formed by dense waters sinking at high latitudes and flowing at depths from approximately 2,000 m to the ocean bottom. These waters take up tracers, such as heat, carbon, and oxygen, while in contact with the atmosphere, and can store them in the deep ocean for time scales of hundreds to thousands of years (Bullister et al., 2013; Talley et al., 2011). In the deep ocean, diapycnal (cross-density) mixing becomes crucial for the closure of the deep branch of the ocean circulation, that is, working to raise dense waters back to shallower depths, and so from there to the surface of the ocean (Munk & Wunsch, 1998; Wunsch & Ferrari, 2004). Such diapycnal mixing, that is, the irreversible transformation of a water parcel's density, is largely driven by the turbulent breaking of internal waves, which in the deep ocean are in large part generated through the interaction of tides with the bottom topography (MacKinnon et al., 2017).

To quantify the role of internal wave-induced diapycnal mixing in the upwelling of dense waters, it is necessary to know (i) the proportion, or local breaking efficiency  $q$ , of internal wave energy which “breaks” locally relative to that which radiates away; and (ii) the turbulent flux coefficient  $\Gamma = \mathcal{M}/\epsilon$ , the ratio of

an appropriate irreversible mixing rate ( $\mathcal{M}$ ) to the rate of turbulent kinetic energy dissipated through frictional heat production ( $\epsilon$ ) (Osborn, 1980; Peltier & Caulfield, 2003). Note that the flux coefficient can be defined as  $\Gamma = \eta/(1 + \eta)$ , where  $\eta = \mathcal{M}/(\mathcal{M} + \epsilon)$  is the (irreversible and instantaneous) mixing efficiency, that is, the ratio of the irreversible mixing rate to the rate by which the turbulence is irreversibly converting kinetic energy. Commonly, particularly in the oceanographic literature,  $\Gamma$  is imprecisely referred to as “mixing efficiency.”

These parameters,  $q$  and  $\Gamma$ , represent the global to local redistribution of wave energy into turbulent mixing and dissipation, as schematically represented in Figures 1a–1c. Due to both lack of knowledge of their variations and for practical reasons, it is customary to assume constant values for both  $q$  and  $\Gamma$ :  $q = 0.3$  (St Laurent et al., 2002; Jayne, 2009) and  $\Gamma = 0.2$  (Osborn, 1980; Mashayek & Peltier, 2013; St Laurent et al., 2002) in parameterizations of deep ocean mixing in coarse resolution ocean and climate models that do not resolve the internal wave field and wave breaking.

The choice of  $q = 0.3$  derives from earlier estimates of the tidal energy flux at a few selected topographic sites (Egbert & Ray, 2003; St Laurent & Garrett, 2002; St Laurent et al., 2002), which inevitably cannot be representative of the global ocean nor can they account for a variety of small-scale processes, such as the interaction of internal waves with small topographic features (Vic et al., 2019). Recent observation- and model-based estimates have highlighted the strong spatial heterogeneity of  $q$  (e.g., Waterhouse et al., 2014; Lefaive et al., 2015; Vic et al., 2019), and idealized model studies have shown that the ocean state is sensitive to the distribution of internal tide energy between the near field and far field (Melet et al., 2016). Thus, a constant value of  $q = 0.3$  does not do justice to the different regimes of internal tide generation and likely induces biases in global circulation models (MacKinnon et al., 2017).

$\Gamma = 0.2$  was actually the empirical upper bound proposed by Osborn (1980), but since then there has been extensive evidence that  $\Gamma$  can vary significantly depending on the properties of the flow (e.g., Moum, 1996; Ruddick et al., 1997; St Laurent & Schmitt, 1999; Smyth & Caldwell, 2001; Mashayek & Peltier, 2013; Salehipour et al., 2016; Gregg et al., 2018). To represent such variability,  $\Gamma$  has often been parameterized (e.g., see Shih et al., 2005; Bouffard & Boegman, 2013) as a nonmonotonic function of the buoyancy Reynolds number, a measure of the turbulence intensity relative to stratification and viscosity, defined as

$$Re_b = \frac{\epsilon}{\nu N^2}, \quad (1)$$

where  $\nu$  is the kinematic viscosity of seawater and  $N^2 = -(g/\rho_0)\partial_z\rho$  is the ocean density stratification where  $\rho_0$  is a reference density and  $g$  the gravitational acceleration. Although it is by no means settled that mixing in stratified turbulence is generically a function of  $Re_b$  (see, e.g., Gregg et al., 2018; Ijichi & Hibiya, 2018; Portwood et al., 2019), there is also strong evidence that the important abyssal mixing process mediated by shear-driven instabilities does indeed vary nonmonotonically with  $Re_b$  (Mashayek, Caulfield, & Peltier, 2017). Previous studies have investigated the sensitivity of the mixing-driven deep overturning circulation to variations in  $\Gamma$  (De Lavergne et al., 2016b; Mashayek, Salehipour, et al., 2017) but without exploring its covariation with other parameters.

Here, we explore the effects of spatially variable  $q$  and  $\Gamma(Re_b)$  on the turbulent mixing that contributes to the regulation of the deep global meridional overturning circulation and also how the *combined* variations of these two parameters modifies the global patterns of upwelling and downwelling of deep waters. In section 2 we present the estimates of internal tides used here and their local breaking efficiency  $q$ . Section 3 describes how to infer diapycnal mixing from the internal wave energy field, while the sensitivity of mixing to spatially variable  $q$  and  $\Gamma(Re_b)$  is presented in section 4. Conclusions are drawn in section 5.

## 2. Internal Tides in the Deep Ocean

Internal waves are generated in the deep ocean by several mechanisms, one of the most important of which is the interaction of tidal currents with the bottom topography (MacKinnon et al. 2017). Barotropic tidal currents in stratified waters interact with the ocean’s seafloor to generate internal tides, that is, internal waves at tidal frequencies. Under the two assumptions of (I) small topographic steepness, that is, that the topographic slope is smaller than the internal wave slope; and (II) small tidal excursion compared to topographic scales, the barotropic-to-baroclinic energy conversion; that is, the rate of internal-tide energy generation, is well predicted by linear theory (Garrett & Kunze, 2007). These two assumptions hold over most of the

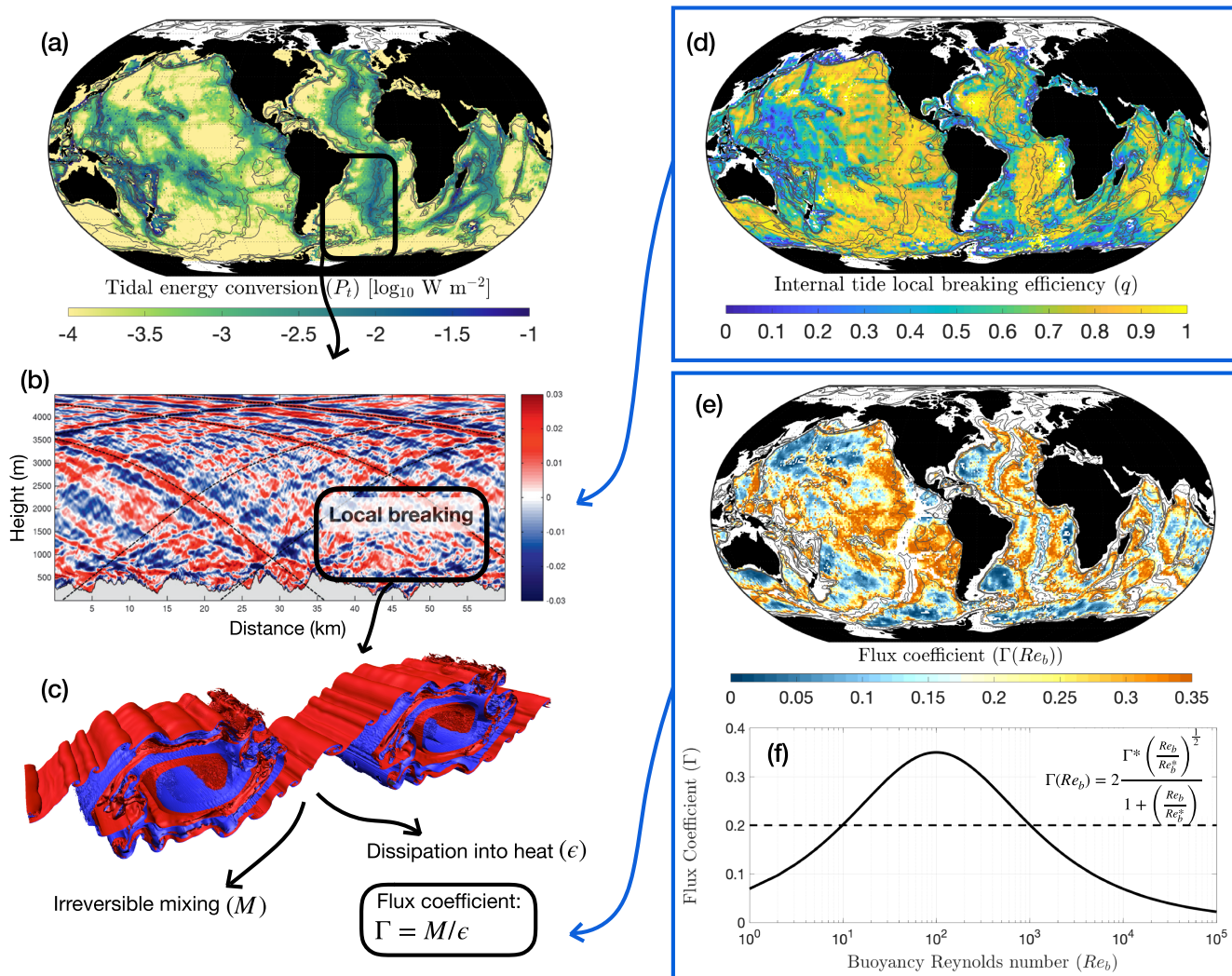


**Figure 1.** (a) Energy conversion into internal tides, reconstructed from Vic et al. (2019). (b) Generation of internal tides over rough topography (the panel shows internal tide velocities [m/s] from numerical simulations, from Nikurashin and Legg, 2011). A fraction of the power in the generated waves,  $(1 - q)$ , radiates away from the generation region, while the remaining fraction  $q$  is converted locally. (c) (from Mashayek, Caulfield, & Peltier, 2017) From each wave breaking event, part of the energy in the generated turbulence is converted into irreversible mixing (with rate  $\mathcal{M}$ ), while the rest is viscously dissipated (with rate  $\epsilon$ ), such that  $\Gamma = \mathcal{M}/\epsilon$ . (d) Internal tide local breaking efficiency  $q(x, y)$ , reconstructed from Vic et al. (2019). (e) Flux coefficient  $\Gamma(Re_b)$  at 3,500 m, using (f) the parameterization of Mashayek, Salehipour, et al. (2017). The maximum flux coefficient ( $\Gamma^* = 0.35$ ) occurs at  $Re_b^* = 100$ ; both values fall within the bound reported in Mashayek, Salehipour, et al. (2017).

deep ocean, and so linear analytical models have been used to estimate the rate of internal tide generation globally (Jayne & Laurent, 2001; St Laurent et al., 2002; Nycander, 2005; Green & Nycander, 2013). Internal tides span a wide range of horizontal and vertical scales, and it is customary to cast them into a set of orthogonal modes whose structure is influenced by the local stratification. This modal decomposition is particularly useful to separate internal tides into two broad families. “Low-mode” (i.e., large-scale) internal tides are able to propagate over thousands of kilometers from their generation site before breaking in the far field (Zhao et al., 2016). Conversely, “high-mode” (i.e., small-scale) internal tides are more prone to local near-field dissipation (St Laurent & Nash, 2004; Vic et al., 2018) and mixing (MacKinnon et al., 2017).

Recently, Vic et al. (2019) computed a global estimate of tidal energy conversion into normal modes. The tidal energy conversion in the deep ocean is shown in Figure 1a for the most energetic tides, that is, the semidiurnal tides ( $M_2$  and  $S_2$ ) and the diurnal tides ( $K_1$ ). Global patterns are consistent with previous estimates, showing enhanced conversion over mid-ocean ridges, seamounts, and continental shelf breaks (Green & Nycander, 2013; Nycander, 2005). The global energy conversion into internal tides from the estimate of

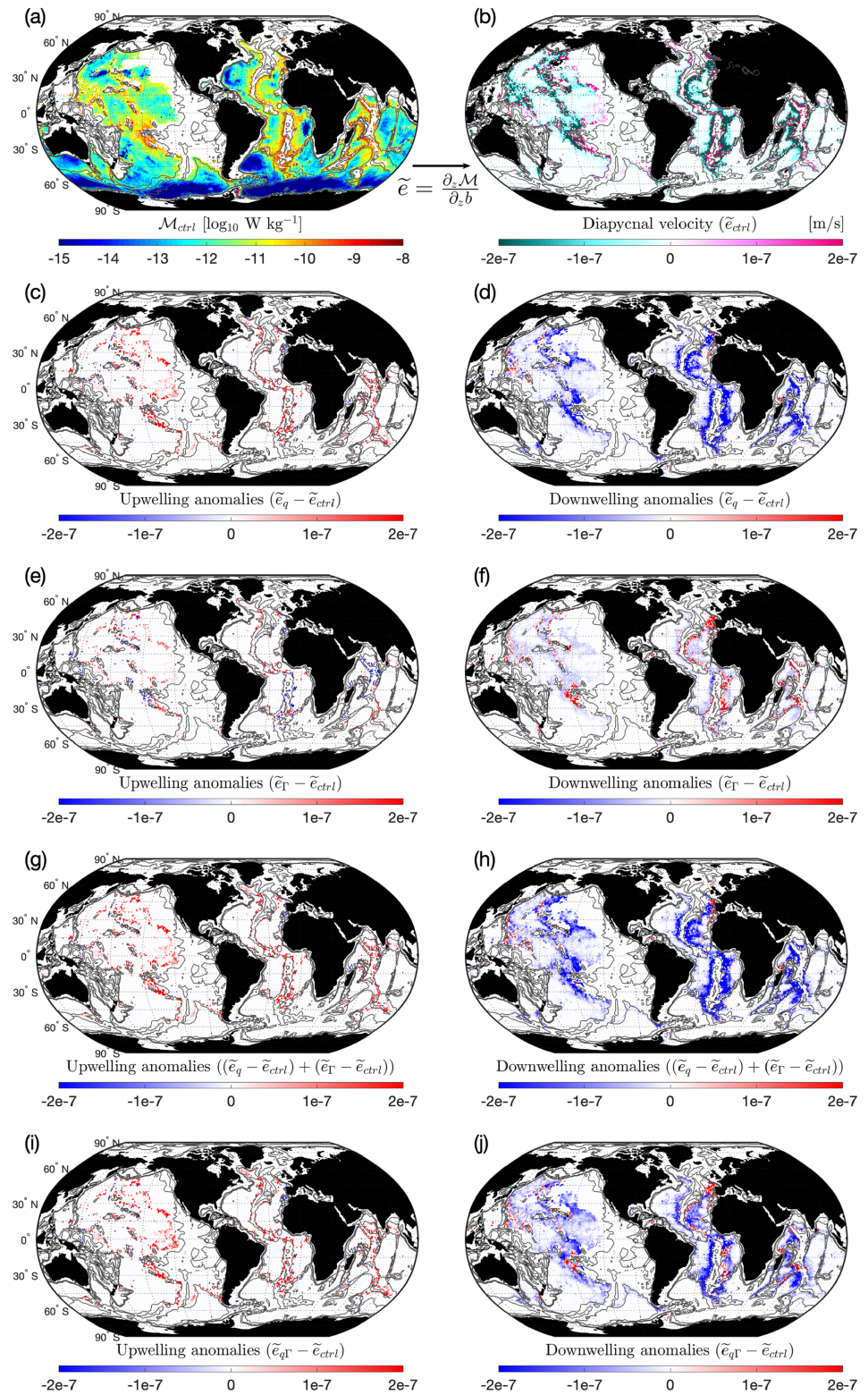


**Figure 2.** (a) Diapycnal mixing (log scale) over the neutral density surface  $\gamma^n = 28.1$  for case (*ctrl*), that is,  $q = 0.3$ ,  $\Gamma = 0.2$ . All the following panels are on the same neutral density surface. (b) Diapycnal velocity  $\tilde{e}$  for case (*ctrl*), with negative velocities (dark cyan) indicating downwelling and positive velocities (magenta) indicating upwelling. Panels (c) and (d), (e) and (f), and (i) and (j) show differences in upwelling (left column) and downwelling (right column) between the different cases and case (*ctrl*). Panels (g) and (h) show the sum of the anomalies of case (q) and case ( $\Gamma$ ) with respect to case (*ctrl*).

Vic et al. (2019) is 0.92 TW, consistent with previous estimates, which suggest that internal tides provide about 1 TW, that is, approximately 50% of the energy required to sustain the deep ocean circulation (Munk & Wunsch, 1998; Jayne and Laurent, 2001). Vic et al. (2019) also used the modal partitioning to separate the portion of internal tides contributing to near-field dissipation (i.e., tides with modes higher than 4, see Vic et al. (2019), for details) from the total energy conversion, hence determining a geographically variable  $q = q(x, y)$  (Figure 1d). Note that the map of  $q(x, y)$  is poorly sensitive to the value of the mode number used to separate the near-field to the far-field mixing, as later discussed in the supporting information (Figure S4). Strikingly,  $q(x, y)$  displays significant geographical variability and equals the perhaps surprisingly large value  $\sim 0.62$  on average. Stemming from the modal partitioning,  $q(x, y)$  is small over steep and narrow ridges, for example, Hawaii Ridge, and seamounts, which generate preferentially low-mode internal tides, leaking energy away. On the contrary,  $q(x, y)$  is much higher over widely spread mid-ocean ridges featuring rough topography (e.g., Mid-Atlantic Ridge) that mostly generate high-mode internal tides. We will use this map of spatially variable  $q(x, y)$  to explore the sensitivity of diapycnal mixing to changes in the local breaking efficiency.

### 3. Irreversible Mixing From Internal Tide Breaking

#### 3.1. Power From Locally Breaking Internal Tides

Figure 1a shows the energy conversion into internal tides in the deep ocean. Assuming such an energy conversion rate decays vertically from the bottom toward the surface with an exponential decay function, motivated by turbulence observations in the deep ocean (St Laurent et al., 2002; Waterhouse et al., 2014), the power locally available to turbulence may be expressed as

$$P_{loc} = qP_t \frac{e^{-(H+z)/\zeta}}{\zeta(1 - e^{-H/\zeta})}, \quad (2)$$

where  $P_t$  is the rate of internal tide generation,  $z$  is the height above the bottom,  $H$  is the total depth of the water column,  $\zeta$  is the vertical decay scale of turbulence, taken to be 500 m, and  $q$  is the local breaking efficiency associated with internal tides. (The impact of a spatially variable  $e$ -folding scale  $\zeta$  is briefly discussed in the supporting information.) Note that we have not taken into account the contribution of radiating internal waves originated in other locations and of other sources of internal waves, such as lee waves or near-inertial waves.

#### 3.2. $\Gamma$ Parameterization

Diapycnal mixing is expected to be small both when the stratification is sufficiently “weak” (compared to the turbulence) so there is little density variation to be homogenized, and when the stratification is sufficiently “strong” to suppress vertical motions and hence mixing. Therefore, it is plausible that there is a range of values of turbulence and stratification within which mixing is more efficient; that is,  $\Gamma$  is larger (De Lavergne et al., 2016b; Mashayek, Salehipour, et al., 2017). Such relations between mixing and the ocean stratification and turbulence are important when inferring  $\mathcal{M}$  from the internal wave energy conversion, but they are not accounted for with a constant flux coefficient. Here, we use the parameterization described in Mashayek, Salehipour, et al. (2017), which assumes the expected nonmonotonic dependence of  $\Gamma$  on the buoyancy Reynolds number, as shown in Figure 1f.

In Figure 1e, we plot a global map of  $\Gamma(Re_b)$  at the depth of 3,500 m, calculated by applying a variable  $q(x, y)$  (Figure 1d) and by using a climatological stratification from the World Ocean Circulation Experiment climatology (Koltermann et al., 2011).  $\Gamma$  increases in the proximity of complex topographic structures but is largest on the ridge’s flanks, rather than at the crest. On the ridge crest, where  $\epsilon$  is the largest, the combination of large values of  $\epsilon$  and the decrease of stratification with depth leads to a larger buoyancy Reynolds number ( $Re_b \sim 1,000$ ) and so to a reduction of the flux coefficient (Figure 1f). A global map of  $Re_b$  is shown in supporting information Figure S1.

#### 3.3. Inferring Mixing

Diapycnal mixing rates are known to be highly spatiotemporally variable (Smyth & Caldwell, 2001; Thorpe, 2007) and are often inferred from estimates of the dissipation rate and knowledge of the flux coefficient

$$\mathcal{M} \approx \overline{w'b'} \approx \Gamma \epsilon, \quad (3)$$

where  $b = -(g/\rho_0)/\delta\rho$  is the buoyancy and  $\overline{w'b'}$  is the turbulent buoyancy flux due to correlations between the turbulent vertical velocity  $w'$  and buoyancy fluctuations  $b'$ , where the fluctuations occur on time scales shorter than the averaging associated with the overbar (Ferrari et al., 2016), taken over a sufficiently long period that reversible and horizontal components of the buoyancy flux are negligible. The power generated by locally breaking waves,  $P_{loc}$ , is converted into either irreversible mixing or into dissipation of turbulent kinetic energy, such that  $P_{loc} = \epsilon + \mathcal{M}$ . The dissipation rate,  $\epsilon$ , is then estimated from  $P_{loc}$  using equation (3):

$$\epsilon = \frac{P_{loc}}{\Gamma + 1}. \quad (4)$$

As  $\Gamma(Re_b)$  and  $Re_b(\epsilon)$ , this equation is solved iteratively using the parameterization shown in Figures 1e and 1f. We first guess  $\Gamma$ , then calculate an estimate of  $\epsilon$ , calculate  $Re_b$ , which is then used to update  $\Gamma$  from the parameterization. This loop is repeated until  $\Gamma$  converges; that is, at each location the variation between the previous estimate and the last one is smaller than  $10^{-6}$ , assuming that variations in  $\Gamma$  of that order are negligible. Note that this iterative process is solved within a few (two to six) iterations, and it is therefore feasible to implement it in climate models. The patterns of  $P_{loc}$  and  $\epsilon$  are shown in the supporting information (Figures S2 and S3).

## 4. Results

The sensitivity of diapycnal mixing to the covariation of  $q$  and  $\Gamma$  is described here by analyzing four distinct cases. The case in which both  $q$  and  $\Gamma$  are constant and equal to the canonical values  $q = 0.3$  and  $\Gamma = 0.2$  is taken to be the control case, (*ctrl*). We first allow  $q(x, y)$  to vary according to Figure 1d while keeping the flux coefficient constant, in a case named ( $q$ ). Then, in a case named ( $\Gamma$ ), we vary the flux coefficient alone (as per Figures 1e and 1f), while keeping  $q$  constant. We vary both parameters to spatially variable  $q(x, y)$  and  $\Gamma(Re_b)$  in a fourth case, named ( $q\Gamma$ ).

### 4.1. Global Patterns of Diapycnal Velocities

The buoyancy flux  $\mathcal{M}$  for case (*ctrl*) is shown in Figure 2a on the neutral density surface  $\gamma^n = 28.1$  (Jackett & McDougall, 1997), which lies on average at the depth of 3,500 m. As will be shown later, this density level corresponds to the peak diapycnal transformation of deep waters, in agreement with previous studies (De Lavergne et al., 2016a; Ferrari et al., 2016; Lavergne et al., 2017; Mashayek, Salehipour, et al., 2017). Note that in the calculation of the buoyancy flux  $\mathcal{M}$  we also include the contribution of geothermal heat flux from the estimate of Davies and Davies (2010).

Mixing is particularly large close to topographic ridges and where the density surface contacts the bottom. However, the net water mass transformation depends on its vertical divergence: If the buoyancy flux is vertically homogeneous, there is no convergence or divergence of water masses and no net water mass transformation. On the contrary, a vertical variation in the buoyancy flux leads to convergence or divergence of water masses. Water hence moves across density surfaces at the diapycnal velocity (Ferrari et al., 2016):

$$\tilde{\mathbf{e}} \approx \frac{\partial_z \mathcal{M}}{\partial_z b}. \quad (5)$$

A positive  $\tilde{\mathbf{e}}$  indicates diapycnal upwelling, that is, water becomes lighter, while a negative  $\tilde{\mathbf{e}}$  indicates diapycnal downwelling; that is, water becomes denser. The diapycnal velocity for case (*ctrl*) is shown in Figure 2b, showing that upwelling is happening along the seafloor (magenta), while downwelling is happening in the ocean interior (dark cyan), as described in previous studies (De Lavergne et al., 2016a; Ferrari et al., 2016). Diapycnal velocities are also shown in Figures 3c and 3d for different cases across a zonal section, highlighting the along-boundary upwelling and interior downwelling pattern.

The differences in diapycnal velocity between the different cases and the (*ctrl*) case are shown in Figures 2c–2j over the neutral density surface  $\gamma^n = 28.1$ . These panels show differences in diapycnal upwelling (left column) and diapycnal downwelling (right column). Positive anomalies in diapycnal upwelling indicate enhanced upwelling, while negative anomalies in diapycnal downwelling indicate enhanced downwelling. Comparing cases (*ctrl*) and ( $q$ ), we find that case ( $q$ ) shows overall larger upwelling (positive anomalies in Figure 2c) and larger downwelling (negative anomalies in Figure 2d), meaning that waters sink in the ocean interior and are raised along the boundaries at faster rates. This is a consequence

of the fact that the spatial average of  $q(x, y)$  is appreciably larger than the (commonly assumed) constant value of  $q = 0.3$ , therefore leading to a larger fraction of waves breaking locally and so to a larger dissipation rate (given that in both cases  $\Gamma$  is held constant). This enhances the buoyancy flux, leading to enhanced upwelling and downwelling. Diapycnal upwelling and downwelling are weaker in case ( $q$ ) only in relatively small regions (e.g. western Pacific), where  $q(x, y)$  is smaller than 0.3.

From an energy perspective, the use of an overall larger  $q$  increases the global rate of energy locally available to turbulence from breaking internal tides (as described by  $P_{loc}$ ). From a global energy conversion rate into internal tides of 0.92 TW, only 0.28 TW is converted locally in the (*ctrl*) case, compared to 0.44 TW in the ( $q$ ) case. If we were going to use a constant  $q$  that would return the same  $P_{loc}$  as in the ( $q$ ) case (which would be  $q_c = \int P_{loc} dA / \int P_t dA = 0.44 / 0.92 \approx 0.48$ ), it would lead to quite significant differences in the diapycnal velocities (shown in supporting information Figure S3). Therefore, while Figures 2c and 2d do not show extensive spatial changes (since  $q(x, y)$  is almost everywhere larger than 0.3), applying a larger but constant value of  $q$  would lead to over/underestimates of the diapycnal velocities, indicating that it is important to take into account also the spatial variations of  $q(x, y)$ .

Figures 2e and 2f show the differences in diapycnal velocities between case ( $\Gamma$ ) and case (*ctrl*). Applying a variable flux coefficient returns overall smaller, but highly spatially variable, changes in the diapycnal velocities. The pattern of  $\Gamma(Re_b)$  depends on a balance between the local turbulence and stratification, as described previously in section 3.2. Changes in  $\Gamma(Re_b)$  consequently lead to changes in the buoyancy flux,  $\mathcal{M} \approx \Gamma \epsilon$ , whose global average for the different scenarios is shown in Figure 3b as a function of height above the bottom. The buoyancy flux is set by the profiles of  $\epsilon$  and  $\Gamma$ . The former exponentially decreases from the bottom (as per equation (2)); the latter, when not constant, is nonmonotonic in the vertical (as discussed and shown in supporting information Figure S5). A variable flux coefficient reduces, on average, the vertical divergence of the buoyancy flux, implying reduced diapycnal velocities, in particular in the first 500 m above the ocean bottom (see later Figure 3).

In Figures 2g and 2h we show the sum of the differences caused by the independent variation of either  $q$  or  $\Gamma$ , that is, the sum of Figures 2c–2e and 2d–2f, respectively. On the other hand, Figures 2i and 2j show the differences between the diapycnal velocities obtained when  $q$  and  $\Gamma$  are varied *in tandem*, using both a variable  $q(x, y)$  and  $\Gamma(Re_b)$  in the case ( $q\Gamma$ ), and the (*ctrl*) case. Comparison between Figures 2g, 2h and 2i, 2j shows the clear nonlinearity of the problem, implying that changes in  $q(x, y)$  and  $\Gamma(Re_b)$  are coupled and that it is therefore needed to change these parameters together. Indeed, changes in  $q(x, y)$  alter both the amount and the spatial variation of power from locally breaking waves  $P_{loc}$ , that is, the power available to drive both turbulent mixing and dissipation, leading to changes in  $Re_b$  and hence in  $\Gamma$ .

With a variable flux coefficient  $\Gamma$  but constant  $q$ , the changes in diapycnal velocities (Figures 2e and 2f) are overall smaller than the equivalent changes found with a variable  $q(x, y)$  and a constant flux coefficient (Figures 2c and 2d). It follows that the differences shown in Figures 2g and 2h are dominated by the changes in  $q$ . On the contrary, when we vary these parameters *in tandem*, the changes in diapycnal velocities (in particular in the downwelling velocities) caused by a variable flux coefficient become substantially more important, and in several places they overcome the changes driven by  $q(x, y)$  (e.g., in western Pacific and the eastern flanks of the Mid-Atlantic Ridge). These anomalies indicate that changes in  $\Gamma(Re_b)$  generically compensate for the increase in available power associated with allowing variable  $q(x, y)$ , with consequences for the strength of the deep ocean circulation and for the exchange of water masses and tracers.

The diapycnal velocities for the cases ( $q$ ) and ( $q\Gamma$ ) are also shown in Figures 3c and 3d along a section at 15°S (Figure 3a). Furthermore, the difference between them is shown in Figure 3e. The along-boundary diapycnal upwelling is overall weaker in case ( $q\Gamma$ ), as highlighted by the predominantly negative anomalies in Figure 3e along the seafloor. Diapycnal downwelling is weaker (and so associated with positive anomalies) in the proximity of topography in the ( $q\Gamma$ ) case, but the thickness of the layer over which significant downwelling takes place increases in this case, and negative anomalies (indicating enhanced downwelling) are found further away from the bottom. Note that these results are sensitive to the vertical decay function of the energy dissipation, and in particular, stratification-dependent decay functions (e.g., Polzin, 2009) could return a different pattern. As described above, these changes can also be described by comparing the buoyancy flux for the different cases (Figure 3b). A variable flux coefficient  $\Gamma$ , especially when in covariation with a variable  $q$ , leads to reduced vertical divergence of the buoyancy flux and so to weaker diapycnal velocities.

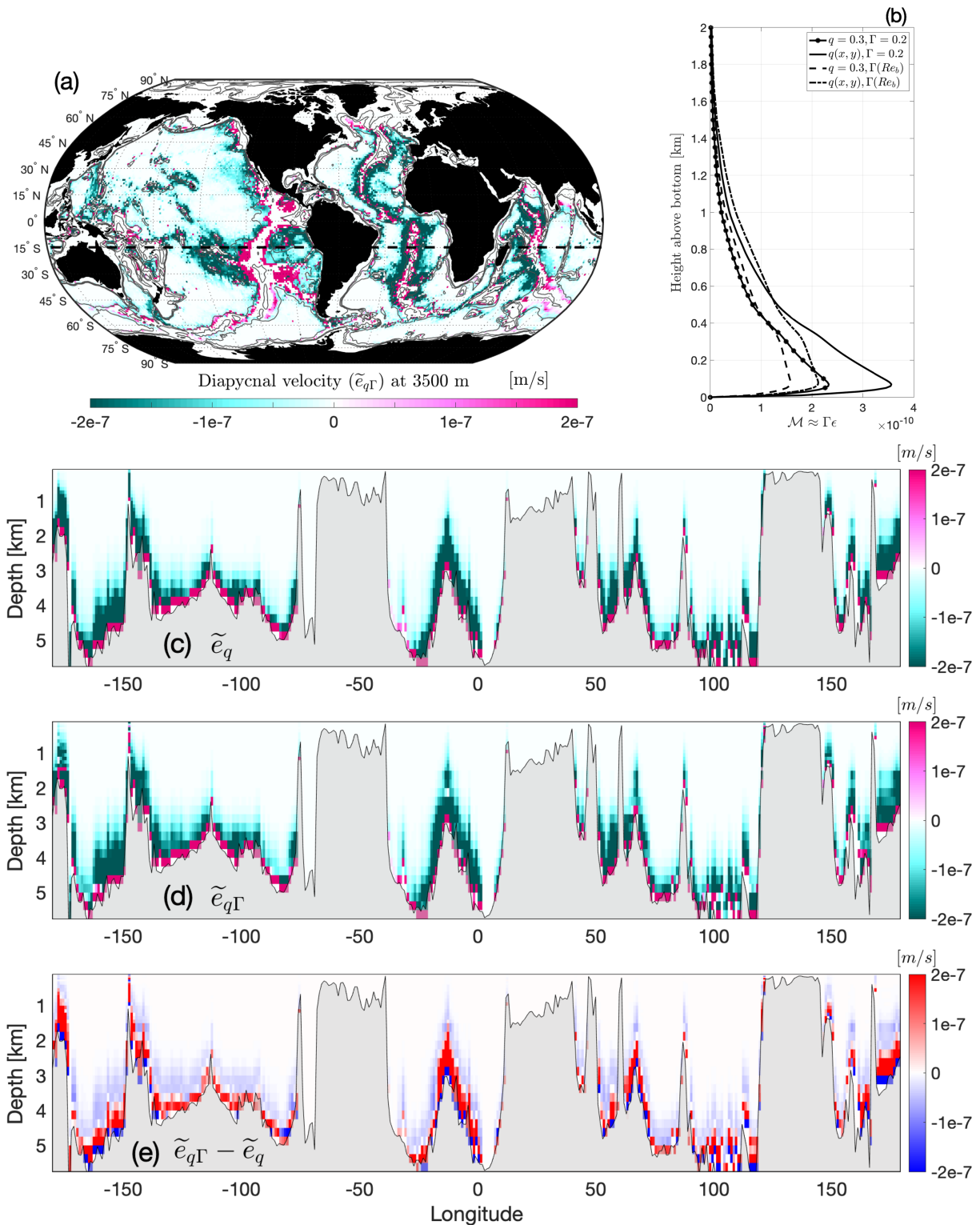


**Figure 3.** (a) Diapycnal velocities at 3,500 m for case ( $q\Gamma$ ). The dashed line indicates the section at 15°S. (b) Globally averaged buoyancy flux for the four cases investigated as a function of height above the bottom. (c, d) Diapycnal velocities across a section at 15°S for cases ( $q$ ) and ( $q\Gamma$ ), respectively. (e) Difference in the diapycnal velocities between cases ( $q\Gamma$ ) and ( $q$ ) (panel d and panel c).

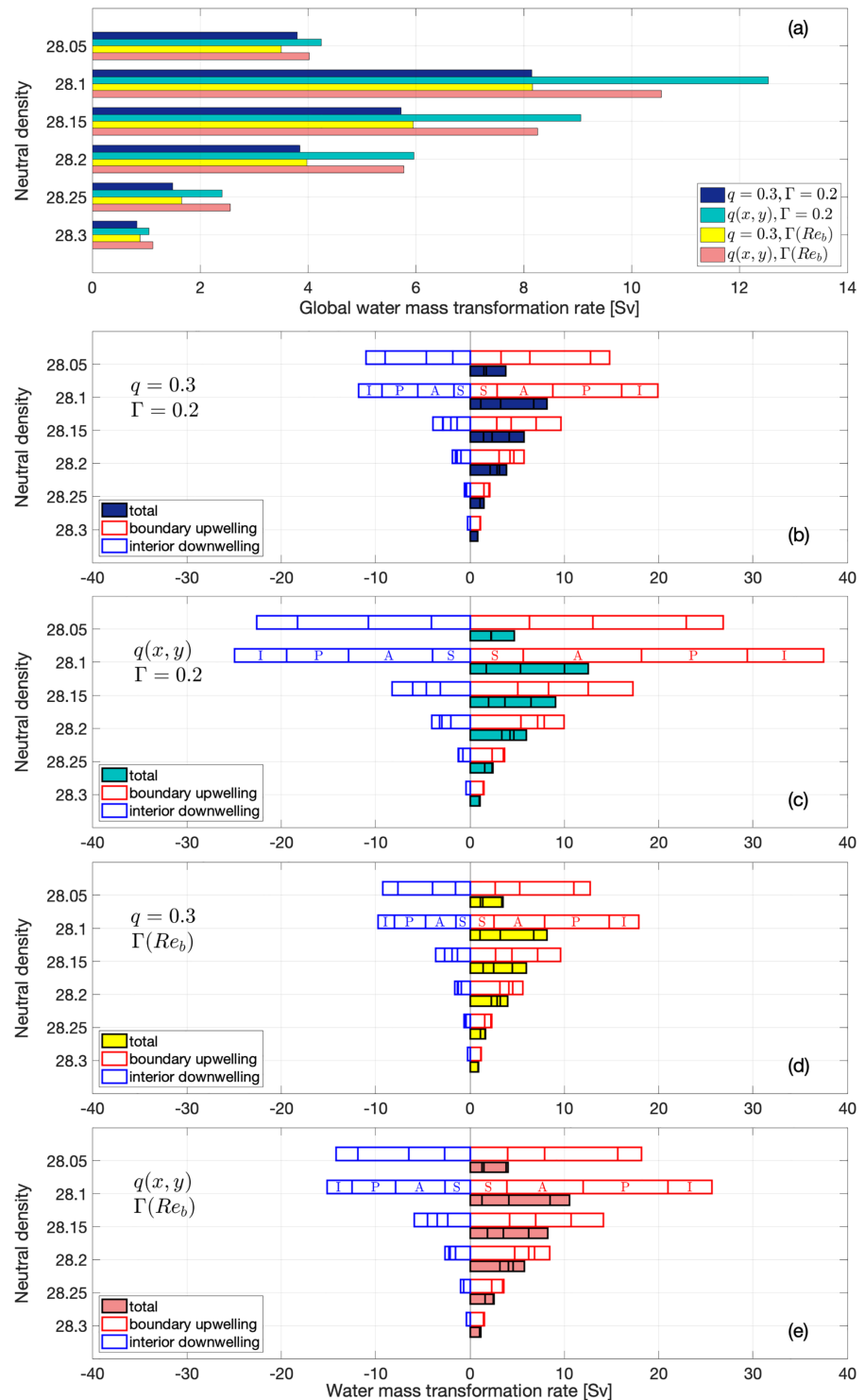


**Figure 4.** (a) Total global water mass transformation rate (i.e., net value between along-boundary upwelling and interior downwelling) for the four cases investigated here. Panels (b)–(e) separate the total water mass transformation rate (filled bars, same colors as panel a) into different ocean basins: Southern Ocean (labeled S); Atlantic Ocean (A); Pacific Ocean (P); and Indian Ocean (I). The Southern Ocean region is defined as the areas south of  $32^\circ\text{S}$ , while the other regions are defined as the areas north of  $32^\circ\text{S}$  in each basin. Transformation rates are labeled by the relevant ocean basin for the neutral density surface  $\gamma^n = 28.1$ . The same ordered arrangement (i.e., S,A,P,I) is also used for the other density surfaces, counting outward away from the  $x$  axis origin, with each basin further separated into (positive) upwelling along boundaries (marked with red bars) and interior downwelling (blue bars).

#### 4.2. Water Mass Transformation Rate

To quantify the effect of the differences in the patterns of upwelling and downwelling on the ocean circulation, and especially on the rising of deep waters back to shallower depths, we calculate the total water mass transformation. For a given density surface, the total water mass transformation is given by the integral of the diapycnal velocity  $\tilde{\mathbf{e}}(\rho)$  over that surface:

$$D(\rho) = - \int_A \tilde{\mathbf{e}}(\rho) \cdot \mathbf{n} \, dA, \quad (6)$$

where  $\mathbf{n}$  is the unit vector normal to the density surface and the minus sign is used such that water mass transformation is positive when water goes from denser to lighter (following Ferrari et al., 2016).

Figure 4a shows the total global water mass transformation, that is, the residual from the sum of the along-boundary upwelling and interior downwelling, for the four cases analyzed here. As expected, the residual is positive, indicating that the net contribution of diapycnal mixing is to transform dense water into lighter water, therefore contributing to raising deep waters back to the surface. For each analyzed neutral density layer, the water mass transformation indicates how much water is transformed into lighter density classes. Note that we report the water mass transformation only for the density classes whose average depth is below  $\sim 2,000$  m as our focus is on the impact of mixing on the deep overturning waters. Also, as we choose a 500-m decay scale, and without accounting for the far-field or background mixing, the water mass transformation rate decays quickly away from the bottom.

The cases analyzed here return an overturning rate of approximately 8–13 Sv, out of which 4 Sv is the peak contribution of geothermal heat flux (not shown), in agreement with previous studies (Adcroft et al., 2001; Scott et al., 2001; Emile-Geay & Madec, 2009). These overturning rates correspond to the deep internal tide-induced circulation, which is naturally smaller than the 20–30 Sv of deep overturning circulation inferred from inverse models (e.g., Lumpkin & Speer, 2007; Talley et al., 2003) or ocean state estimates (e.g., Cessi, 2019), which inherently account for the contribution of several other processes, such as the far-field mixing (see, e.g., De Lavergne et al., 2016b, for an estimate of the far-field mixing contribution), boundary turbulence due to nonpropagating processes, lee waves, and near-inertial waves. Moreover, the overturning rate may be sensitive to the uncertainty in  $q(x, y)$  and to the specific values of  $\Gamma^*$  and  $Re_b^*$  used in the parameterization of  $\Gamma(Re_b)$ , both of which are discussed in the supporting information. The overturning rate is also sensitive to the vertical function of energy dissipation (e.g., De Lavergne et al., 2016a, 2016b). Stratification-dependent decay functions have been proposed (e.g., Polzin, 2009), but the exponential decay function with an  $e$ -folding scale of 500 m used here (equation (2)) has been shown to match well with observations of turbulence in the deep ocean (St Laurent et al., 2002). The impact of a variable  $e$ -folding is discussed in the supporting information (Figures S6–S8).

Figures 4b–4e show the distinct contribution of along-boundary upwelling (red bars) and interior downwelling (blue bars) to the net water mass transformation, shown by the filled bars (color coded as in Figure 4a). Each bar also shows the contribution of the different ocean basins to the water mass transformation, where the Atlantic, Pacific, and Indian basins' contributions are calculated only up to  $32^\circ\text{S}$ , and the Southern Ocean is considered a distinct region. For all cases, both the partial (i.e., the upwelling or downwelling) and the net rates of water mass transformation peak at  $\gamma^n = 28.1$ , the neutral density surface with the largest area of contact with the bottom (De Lavergne et al., 2016a; Lavergne et al., 2017). At  $\gamma^n = 28.1$ , the Pacific and Atlantic Oceans are the main contributors, while the Southern Ocean dominates the water mass transformation for denser density classes ( $\gamma^n > 28.2$ ), which are mainly confined south of  $32^\circ\text{S}$ .

Case ( $q$ ) returns much larger rates of upwelling and downwelling, up to 50–100% larger than the other cases, consistently with the results shown in Figures 4c and 4d. These differences lead to a 20–25% larger net water mass transformation, perhaps unsurprisingly given the larger fraction of internal wave energy spent locally. Cases ( $ctrl$ ) and ( $\Gamma$ ), on the other hand, return similar partial and net water mass transformation rates, suggesting that the positive and negative anomalies in the diapycnal velocities driven by a variable flux coefficient (Figures 2e and 2f) almost perfectly cancel out. The covariation of  $q(x, y)$  and  $\Gamma(Re_b)$  returns an overall net water mass transformation quite similar to the net water mass transformation returned by case ( $q$ ). Despite this similarity, Figure 4e shows that case ( $q\Gamma$ ) returns smaller upwelling and downwelling rates, consistent with and confirming what may be deduced from Figures 2i, 2j, and 3b, that is, that a variable flux coefficient  $\Gamma$  compensates for the increase in available power associated with a variable  $q(x, y)$ . These results

indicate that the water mass transformation rates are highly sensitive to the choices of  $q$  and  $\Gamma$  in nontrivial ways and that the two parameters should be varied together to avoid spurious overestimation of the rates of diapycnal upwelling and downwelling.

## 5. Summary and Conclusions

We have investigated the sensitivity of internal tide-driven mixing across the deep meridional overturning circulation to spatially variable local breaking efficiency  $q$  and turbulent flux coefficient (“mixing efficiency”)  $\Gamma$ , parameters representing the global to local energy pathway from internal waves to diapycnal mixing. In four distinct cases, we investigated first the independent effect of a geographically variable local breaking efficiency  $q(x, y)$  compared to the commonly used constant value  $q = 0.3$ , and of a spatially variable flux coefficient  $\Gamma(\epsilon/\nu N^2)$  (parameterized following Mashayek, Salehipour, et al., 2017) compared to the canonical constant value  $\Gamma = 0.2$ . We then investigated the combined effect of using geographically variable parameters.

Our results show that a covariation of  $q$  and  $\Gamma$  has important consequences on both the geographical variations of the diapycnal velocity, (i.e., on the patterns of upwelling and downwelling of water masses) and on the water mass transformation rate. We show that diapycnal mixing is highly sensitive to the choice of  $q$  and  $\Gamma$  and responds in nonlinear ways to parameter covariation. In particular, changing only  $q$  while keeping  $\Gamma$  constant returns much larger values of both upwelling and downwelling and a larger total water mass transformation. A variable  $q(x, y)$ , whose average value is appreciably larger than  $q = 0.3$ , leads to an increase of energy available to turbulence. However, when applying a variable flux coefficient  $\Gamma(Re_b)$ , the increase in energy is partially compensated by changes in the flux coefficient, indicating that the two parameters should be covaried to avoid overestimation of the rates of diapycnal upwelling/downwelling and the water mass transformation rate.

It is crucial to get a correct representation of the spatial distribution of diapycnal mixing to represent the exchange of water masses and tracers accurately across the density surfaces of the deep overturning circulation and so correctly quantify the role of diapycnal mixing in the closure of the deep circulation and in the global redistribution of tracers. Therefore, we believe that it is now timely to implement spatially variable local dissipation efficiency and flux coefficient parameterizations to move toward a more accurate representation of the patterns of diapycnal upwelling and downwelling in ocean and climate models.

## Acknowledgments

Data sets for this research are available online (<https://data.mendeley.com/datasets/35fjmfw3x7/2>). L. C. thanks support from the Clarendon Scholarship and the U.K. Natural Environment Research Council (NERC) via the DTP in Environmental Research (NE/L002612/1). The research activity of C.P.C. was supported by EPSRC Programme Grant EP/K034529/1 entitled ‘Mathematical Underpinnings of Stratified Turbulence’. A.M. acknowledges funding from the NERC IRF fellowship grant NE/P018319/1. C.V. was supported by the NERC RidgeMix project (NE/L004216/1). The authors are grateful to the two anonymous reviewers for constructive and insightful comments on the manuscript.

## References

- Adcroft, A., Scott, J. R., & Marotzke, J. (2001). Impact of geothermal heating on the global ocean circulation. *Geophysical Research Letters*, 28, 1735–1738. <https://doi.org/10.1029/2000GL012182>
- Bouffard, D., & Boegman, L. (2013). A diapycnal diffusivity model for stratified environmental flows. *Dynamics of Atmospheres and Oceans*, 61, 14–34.
- Bullister, J. L., Rhein, M., & Mauritzen, C. (2013). *Ocean circulation and climate—A 21st century perspective, chapter 1*. Kidlington, U.K.: Academic Press. <https://doi.org/10.1016/B978-0-12-391851-2.00001-5>
- Cessi, P. (2019). The global overturning circulation. *Annual Review of Marine Science*, 11, 249–270.
- Davies, J., & Davies, D. (2010). Earth’s surface heat flux. *Solid Earth*, 1, 5–24.
- De Lavergne, C., Madec, G., Le Sommer, J., Nurser, A., & Naveira Garabato, A. (2016a). The impact of a variable mixing efficiency on the abyssal overturning. *Journal of Physical Oceanography*, 46, 663–681.
- De Lavergne, C., Madec, G., Le Sommer, J., Nurser, A. G., & Naveira Garabato, A. C. (2016b). On the consumption of antarctic bottom water in the abyssal ocean. *Journal of Physical Oceanography*, 46(2), 635–661.
- De Lavergne, C. D., Madec, G., Roquet, F., Holmes, R., & McDougall, T. (2017). Abyssal ocean overturning shaped by seafloor distribution. *Nature*, 551, 181–186.
- Egbert, G. D., & Ray, R. D. (2003). Semi-diurnal and diurnal tidal dissipation from TOPEX Poseidon altimetry. *Geophysical Research Letters*, 30(17), 1907. <https://doi.org/10.1029/2003GL017676>
- Emile-Geay, J., & Madec, G. (2009). Geothermal heating, diapycnal mixing and the abyssal circulation. *Ocean Science*, 5(2), 203–217.
- Ferrari, R., Mashayek, A., McDougall, T., Nikurashin, M., & Champin, J.-M. (2016). Turning ocean mixing upside down. *Journal of Physical Oceanography*, 46, 2239–2261.
- Garrett, C., & Kunze, E. (2007). Internal tide generation in the deep ocean. *Annual Review of Fluid Mechanics*, 39, 57–87.
- Green, J., & Nycander, J. (2013). A comparison of tidal conversion parameterizations for tidal models. *Journal of Physical Oceanography*, 43, 104–119.
- Gregg, M., D’Asaro, E., Riley, J., & Kunze, E. (2018). Mixing efficiency in the ocean. *Annual Review of Marine Science*, 10, 443–473.
- Ijichi, T., & Hibiya, T. (2018). Observed variations in turbulent mixing efficiency in the deep ocean. *Journal of Physical Oceanography*, 48(8), 1815–1830.
- Jackett, D., & McDougall, T. (1997). A neutral density variable for the world’s oceans. *Journal of Physical Oceanography*, 27, 237–263.
- Jayne, S. (2009). The impact of abyssal mixing parameterizations in an ocean general circulation model. *Journal of Physical Oceanography*, 39(7), 1756–1775.

- Jayne, S., & Laurent, L. S. (2001). Parameterizing tidal dissipation over rough topography. *Geophysical Research Letters*, *28*, 811–814. <https://doi.org/10.1029/2000GL012044>
- Koltermann, K., Gouretski, V., & Jancke, K. (2011). Hydrographic Atlas of the World Ocean Circulation Experiment (WOCE): Volume 3: Atlantic Ocean. International WOCE Project Office.
- Lefauve, A., Muller, C., & Melet, A. (2015). A three-dimensional map of tidal dissipation over abyssal hills. *Journal of Geophysical Research: Oceans*, *120*, 4760–4777. <https://doi.org/10.1002/2014JC010598>
- Lumpkin, R., & Speer, K. (2007). Global ocean meridional overturning. *Journal of Physical Oceanography*, *37*, 2550–2562.
- MacKinnon, J., Alford, M. H., Ansong, J. K., Arbic, B. K., Barna, A., Briegleb, B. P., et al. (2017). Climate process team on internal wave-driven ocean mixing. *American Meteorological Society*, *98*, 2429–2454.
- Mashayek, A., Caulfield, C. P., & Peltier, W. (2017). Role of overturns in optimal mixing in stratified mixing layers. *Journal of Fluid Mechanics*, *826*, 522–552.
- Mashayek, A., & Peltier, W. (2013). Shear induced mixing in geophysical flows: Does the route to turbulence matter to its efficiency? *Journal of Fluid Mechanics*, *725*, 216–261.
- Mashayek, A., Salehipour, H., Bouffard, D., Caulfield, C. P., Ferrari, R., Nikurashin, M., et al. (2017). Efficiency of turbulent mixing in the abyssal ocean circulation. *Geophysical Research Letters*, *44*, 6296–6306. <https://doi.org/10.1002/2016GL072452>
- Melet, A., Legg, S., & Hallberg, R. (2016). Climatic impacts of parameterized local and remote tidal mixing. *Journal of Climate*, *29*(10), 3473–3500.
- Moum, J. N. (1996). Efficiency of mixing in the main thermocline. *Journal of Geophysical Research*, *101*(C5), 12,057–12,069.
- Munk, W., & Wunsch, C. (1998). Abyssal recipes II: Energetics of tidal and wind mixing. *Deep Sea Research Part I: Oceanographic Research Papers*, *45*(12), 1977–2010.
- Nikurashin, M., & Legg, S. (2011). A mechanism for local dissipation of internal tides generated at rough topography. *Journal of Physical Oceanography*, *41*(2), 378–395.
- Nycander, J. (2005). Generation of internal waves in the deep ocean by tides. *Journal of Geophysical Research*, *110*, C10028. <https://doi.org/10.1029/2004JC002487>
- Osborn, T. (1980). Estimates of the local-rate of vertical diffusion from dissipation measurements. *Journal of Physical Oceanography*, *10*, 83–89.
- Peltier, W., & Caulfield, C. P. (2003). Mixing efficiency in stratified shear flows. *Annual Review of Fluid Mechanics*, *35*(1), 135–167.
- Polzin, K. L. (2009). An abyssal recipe. *Ocean Modelling*, *30*(4), 298–309.
- Portwood, G. D., de Bruyn Kops, S., & Caulfield, C. P. (2019). Asymptotic dynamics of high dynamic range stratified turbulence. *Physical Review Letters*, *122*(19), 194,504.
- Ruddick, B., Walsh, D., & Oakey, N. (1997). Variations in apparent mixing efficiency in the north atlantic central water. *Journal of Physical Oceanography*, *27*(12), 2589–2605.
- Salehipour, H., Peltier, W., Whalen, C., & MacKinnon, J. (2016). A new characterization of the turbulent diapycnal diffusivities of mass and momentum in the ocean. *Geophysical Research Letters*, *43*, 3370–3379. <https://doi.org/10.1002/2016gl068184>
- Scott, J. R., Marotzke, J., & Adcroft, A. (2001). Geothermal heating and its influence on the meridional overturning circulation. *Journal of Geophysical Research*, *106*, 31,141–31,154. <https://doi.org/10.1029/2000JC000532>
- Shih, L. H., Koseff, J. R., Ivey, G. N., & Ferziger, J. H. (2005). Parameterization of turbulent fluxes and scales using homogeneous sheared stably stratified turbulence simulations. *Journal of Fluid Mechanics*, *525*, 193–214.
- Smyth, W., & Caldwell, D. (2001). The efficiency of mixing in turbulent patches: Inferences from direct simulations and microstructure observations. *Journal of Physical Oceanography*, *31*, 1969–1992.
- St Laurent, L., & Garrett, C. (2002). The role of internal tides in mixing the deep ocean. *Journal of Physical Oceanography*, *32*(10), 2882–2899.
- St Laurent, L., & Nash, J. D. (2004). An examination of the radiative and dissipative properties of deep ocean internal tides. *Deep Sea Research Part II: Topical Studies in Oceanography*, *51*(25–26), 3029–3042.
- St Laurent, L., & Schmitt, R. W. (1999). The contribution of salt fingers to vertical mixing in the North Atlantic Tracer Release Experiment. *Journal of Physical Oceanography*, *29*(7), 1404–1424.
- St Laurent, L., Simmons, H., & Jayne, S. (2002). Estimating tidally driven mixing in the deep ocean. *Geophysical Research Letters*, *29*, 21-1–21-4. <https://doi.org/10.1029/2002GL015633>
- Talley, L. D., Pickard, G. L., Emery, W. J., & Swift, J. H. (2011). *Descriptive Physical Oceanography*, (p. 555). Kidlington, U.K.: Academic Press.
- Talley, L. D., Reid, J. L., & Robbins, P. E. (2003). Data-based meridional overturning streamfunctions for the global ocean. *Journal of Climate*, *16*(19), 3213–3226.
- Thorpe, S. (2007). *An introduction to ocean turbulence*. Cambridge, UK: Cambridge University Press.
- Vic, C., Naveira Garabato, A. C., Green, J. M., Waterhouse, A. F., Zhao, Z., Melet, A., et al. (2019). Deep-ocean mixing driven by small-scale internal tides. *Nature Communications*, *10*, 2099.
- Vic, C., Naveira Garabato, A. C., Green, J. M., Spingys, C., Forryan, A., Zhao, Z., & Sharples, J. (2018). The lifecycle of semidiurnal internal tides over the northern mid-atlantic ridge. *Journal of Physical Oceanography*, *48*(1), 61–80.
- Waterhouse, A., MacKinnon, J., Nash, J., Alford, M., Kunze, E., Simmons, H., et al. (2014). Global patterns of diapycnal mixing from measurements of the turbulent dissipation rate. *Journal of Physical Oceanography*, *44*, 1854–1872.
- Wunsch, C., & Ferrari, R. (2004). Vertical mixing, energy, and the general circulation of the oceans. *Annual Review of Fluid Mechanics*, *36*, 281–314.
- Zhao, Z., Alford, M. H., Girton, J. B., Rainville, L., & Simmons, H. L. (2016). Global observations of open-ocean mode-1 M2 internal tides. *Journal of Physical Oceanography*, *46*(6), 1657–1684.